Dark-Field Tomography of an Attenuating Object Using Intrinsic X-Ray Speckle-Tracking

S. J. Alloo[a], D. M. Paganin[b], K. S. Morgan[b], M. J. Kitchen[b], A. W. Stevenson[c], S. C. Mayo[d], H. T. Li[e], B. M. Kennedy[f], A. Maksimenko[c], J. Bowden[d], and K. M. Pavlov[a, b, g]

[a]School of Physical and Chemical Sciences, University of Canterbury, Christchurch, 8041, New Zealand
[b]School of Physics and Astronomy, Monash University, Victoria 3800, Australia
[c]Australian Synchrotron, ANSTO, Clayton, Victoria 3168, Australia
[d]Commonwealth Scientific and Industrial Research Organisation, Clayton, Victoria 3168, Australia
[e]School of Mathematics, University of Canterbury, Christchurch, 8041, New Zealand
[f]School of Earth and Environment, University of Canterbury, Christchurch, 8041, New Zealand
[g]University of New England, Armidale, New South Wales 2351, Australia

ABSTRACT

Purpose: To investigate how an intrinsic speckle-tracking approach to speckle-based X-ray imaging technique can be used to extract an object's effective dark-field signal, which is capable of providing object information in three dimensions.

Approach: The effective dark-field signal was extracted using a Fokker-Planck type formalism, which models the deformations of illuminating reference-beam speckles due to both coherent and diffusive scatter from the sample. We here assumed that (a) small-angle scattering fans at the exit surface of the sample are rotationally symmetric, and (b) the object has both attenuating and refractive properties. The associated inverse problem, of extracting the effective dark-field signal, was numerically stabilised using a "weighted determinants" approach.

Results: Effective dark-field projection images are presented, as well as the dark-field tomographic reconstructions of the wood sample. Dark-field tomography was performed using a filtered-back projection reconstruction algorithm. The dark-field tomographic reconstructions of the wood sample provided complementary, and otherwise inaccessible, information to augment the phase-contrast reconstructions, which were also computed.

Conclusions: An intrinsic speckle-tracking approach to speckle-based imaging can tomographically reconstruct an object's dark-field signal at a low sample exposure and with a simple experimental set-up. The obtained dark-field reconstructions have image quality comparable to alternative X-ray dark-field techniques.

Keywords: Dark Field Computed Tomography, Speckle X-ray Imaging, Intrinsic Speckle Tracking

1. INTRODUCTION

X-rays have been utilized in a variety of applications since their discovery by Röntgen.[1] Their ability to pass through matter makes X-rays highly useful in a broad range of applications, particularly in medical imaging. X-rays are attenuated, scattered, and refracted when traversing a material. As a result, the wavefield at the exit surface of the object contains encoded information regarding that object. X-ray imaging directly visualises differing densities, and therefore refractive indices, of materials within a sample. The refractive index for X-rays

Further author information: (Send correspondence to S. J. Alloo)
S. J. Alloo: samantha.alloo@pg.canterbury.ac.nz,
K. M. Pavlov: konstantin.pavlov@canterbury.ac.nz

travelling through matter is given as $n(\mathbf{r}) = 1 - \delta(\mathbf{r}) + i\beta(\mathbf{r})$, where $\mathbf{r}$ is the position vector, and $\delta(\mathbf{r})$ and $\beta(\mathbf{r})$ describe refraction and attenuation of the X-ray beam, respectively. In many X-ray imaging techniques, it is these functions that provide the relative image contrast, for example conventional radiography is attenuation-based imaging, and hence depends on $\beta(\mathbf{r})$.

Phase-contrast imaging (PCI)[2] is an X-ray imaging technique that exploits the refraction of X-rays in material. PCI is especially useful for imaging objects that are weakly attenuating, e.g. soft tissues in mammography. Propagation-based phase-contrast imaging (PB-PCI)[3–6] is a PCI technique that achieves phase-contrast by making use of sufficiently spatially-coherent illumination and subsequent downstream free-space propagation of the exit-surface wavefront. PB-PCI is a refraction- and attenuation-based radiography technique, which is both convenient and non-invasive, allowing the study of samples at micrometre and sub-micrometre length scales. The downstream propagation in PB-PCI allows the extraction of phase information, relating to $\delta(\mathbf{r})$, via suitable phase-retrieval algorithms. This phase information is lost in attenuation-based X-ray imaging techniques. Paganin *et al.*[7] demonstrated a simple phase-retrieval algorithm for a single-material object using PB-PCI, which is based on the transport-of-intensity equation.[8]

Some methods achieve phase-contrast by introducing additional optical elements, for example, grating-based PCI,[9–16] Bonse-Hart interferometry,[17–19] edge-illumination PCI,[20,21] and analyser-based PCI.[22–26] Speckle-based X-ray imaging (SBXI), first introduced in 2012 by Berujon *et al.*[27] and Morgan *et al.*,[28] uses a spatially random mask placed between the X-ray source and detector (see Fig. 1). This mask acts as a random phase and intensity modulator to generate a near-field speckle pattern. In this technique, information regarding the sample is inferred by studying how the speckles, first measured in the absence of the object, are altered by the introduction of the object. Using such an approach, SBXI is capable of reconstructing phase gradients, attenuation, and small-angle scattering information.[29]

Spatial resolution in PCI is restricted by the finite number and size of pixels in the detector. As a result, micro-structure smaller than the size of the pixel cannot be resolved directly. Dark-field (DF) X-ray imaging provides coarse-grained information about such spatially-unresolved microstructure. DF thereby enables complementary structural information to be obtained at sub-pixel scales. Image contrast in DF imaging is generated by position-dependent small-angle X-ray scattering (SAXS) of the incident beam by the sample. SAXS[30] is the diffusive scattering of an X-ray beam from unresolved microstructures that are smaller than the width of a pixel, and are found within an object. This position-dependent SAXS influences the measured PCI data, leading to the associated inverse problem[31] of how information regarding the spatially-unresolved microstructure (e.g. a position-dependent correlation length) may be inferred from one or more measured PCI images.

Currently, there are a variety of DF-PCI techniques, e.g. propagation-based DF-PCI,[32,33] grating-based DF-PCI,[34–37] edge-illumination DF-PCI,[38,39] and analyzer-based DF-PCI.[26,40–43] Grating-based PCI has regular gratings placed between the source and detector, for example, the so-called Talbot-Lau interferometer reported by David *et al.* and Momose *et al.*[9,10] In such techniques, the attenuation, differential phase and DF signal can be extracted by measuring the intensity variations caused by introducing the sample in the path of the beam. However, to do so, several different image acquisitions are required to reconstruct a single projection. This is done using different transverse positions of the gratings, relative to one another. Single-grating-based methods have also been reported,[44,45] aiming to reduce the X-ray exposure relative to multi-grating-based approaches. Analyzer-based imaging, similarly to grating-based imaging, requires multiple image acquisitions to reconstruct a single projection of the object. In this technique, an analyzer crystal is introduced to selectively measure angular components of the X-ray beam. Kitchen *et al.*[46–48] and Ando *et al.*[42] used a Laue geometry, to simultaneously collect transmitted and diffracted images, to reconstruct both the absorption and phase images in a single exposure. As a result, both the exposure time and radiation dose were considerably reduced compared to alternative techniques that rotate the analyzer crystal.

SBXI techniques are also capable of extracting DF images, through speckle tracking.[49–51] Berujon and Ziegler[51] use "X-ray Speckle-Vector Tracking" (XSVT), and Zdora *et al.*[49] employ the formalism of "Unified Modu-

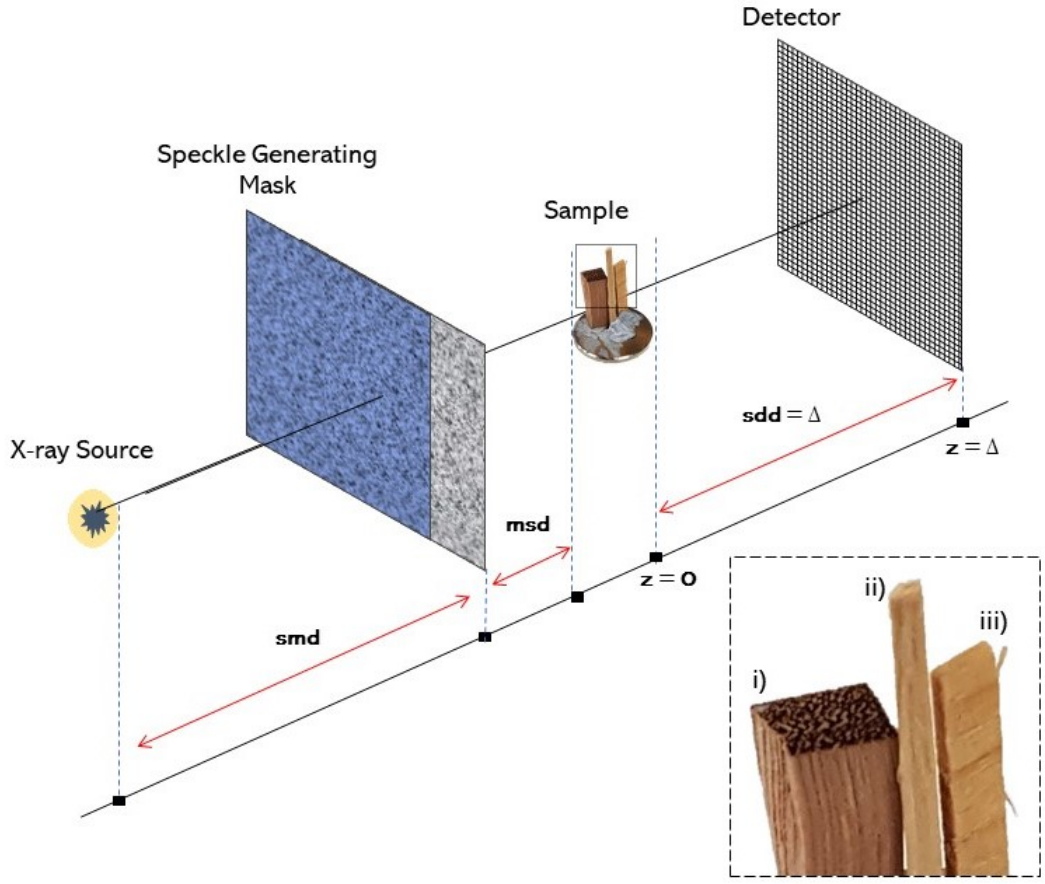

Figure 1. *Schematic of Speckle-Based X-ray Imaging (SBXI) experimental setup. Here, smd is the source-to-mask distance, msd is the mask-to-sample distance, and sdd = Δ is the sample-to-detector distance.*

lated Pattern Analysis" (UMPA). XSVT and UMPA alike apply an explicit, pixel-wise tracking approach to extract the DF signal by analysing multiple SBXI images. However, single-image multimodal recovery is also possible using a correlation based approach.[28,50] Pavlov *et al.* recently developed "Multimodal Intrinsic Speckle-Tracking" (MIST)[52,53], an algorithm able to retrieve a sample's DF signal in SBXI. MIST[52] utilizes intrinsic speckle-tracking within a SBXI set-up to recover an object's phase and DF signal simultaneously, in a deterministic manner. MIST combines a Fokker-Planck[32,54,55] description of paraxial X-ray optics with a geometric-flow formalism for X-ray speckle tracking.[56] The MIST[52] formalism only requires two sets of projection data, for two different transverse positions of the mask, suggesting that the technique may be suitable for clinical applications where dose should be minimised. DF images have proven highly advantageous in the study of soft tissues,[57] and the success of SBI techniques in PCXI has also been highlighted.[58]

The speckle-tracking variant of obtaining the DF signal published by Pavlov *et al.*[52] assumes that (a) the sample is non-attenuating, and (b) the position-dependent SAXS fans that emanate from the exit surface of the object are rotationally symmetric. Here, we extend the MIST formalism[52] to consider a monomorphous attenuating object, while maintaining the assumption of rotationally-symmetric SAXS fans. Such generalizations are crucial for the broader utility of this technique—e.g. in possible future applications to disciplines such as metallurgy, paleontology, soils science and structural failure prediction—since typical samples in such contexts are often strongly attenuating.

2. THEORY

Here we extend the MIST[52] formalism to the case of a monomorphous attenuating object, by first formulating the forward problem and then solving the corresponding inverse problem.[31] The forward-finite-difference Fokker-Planck equation is first obtained, which can be used to model optical energy conservation as the speckles are formed and then deformed due to propagation through a SAXS-inducing object. The inverse problem for a monomorphous attenuating object is then considered, aiming to retrieve both (a) the effective-DF signal and (b) projected thickness (which can be related to the object-induced phase shifts). We also consider two approaches to numerically stabilise the mildly-ill-posed inverse problem.

2.1 Scalar-Diffusion Fokker-Planck Formalism for X-ray Speckle-Tracking: Monomorphous Attenuating Object Approximation

We begin by assuming that a monomorphous attenuating object is placed in a spatially-well-resolved reference speckle field, as in Fig. 1. The reference speckle field, together with the corresponding images in the presence of the sample, obey the Fokker-Planck[55] generalisation[32,54] of the geometric flow formalism[56] for speckle-tracking. Now, following Pavlov *et al.*,[52] and Paganin and Morgan,[32,54] we have the Fokker-Planck equation for SBXI, which models coherent flow and diffusive flow for a phase object described by its phase shift, $\phi_{\text{ob}}(\mathbf{r})$, and effective scalar diffusion coefficient, $D_{\text{eff, Phase}}(\mathbf{r};\Delta)$, as:

$$I_R(\mathbf{r}) - I_S(\mathbf{r}) = \frac{\Delta}{k}\nabla_\perp \cdot [I_R(\mathbf{r})\nabla_\perp \phi_{\text{ob}}(\mathbf{r})] - \Delta\nabla_\perp^2 \left[D_{\text{eff, Phase}}(\mathbf{r};\Delta) I_R(\mathbf{r})\right]. \tag{1}$$

This expression relates the reference speckle image intensity, $I_R(\mathbf{r})$, obtained with no sample in the beam, to the encoded form of the speckle image, $I_S(\mathbf{r})$, which is obtained in the presence of the sample. Here, $(\mathbf{r}) \equiv (x, y)$ denote Cartesian coordinates in planes perpendicular to the optical axis z, Δ is the sample-to-detector distance, k is the wavenumber of the X-rays, $\nabla_\perp = (\partial/\partial x, \partial/\partial y)$ is the gradient operator in the (x, y) plane, and $\nabla_\perp^2$ is the transverse Laplacian operator.

Next, we consider Eqn. (55) from Pavlov *et al.*,[58] which gives the variation in registered intensity of a well resolved speckle field due to an attenuating object as:

$$\frac{I_S}{I_R} \approx I_{\text{ob}}(\mathbf{r}) - \frac{\Delta}{k}\nabla_\perp \cdot [I_{\text{ob}}(\mathbf{r})\nabla_\perp \phi_{\text{ob}}(\mathbf{r})]. \tag{2}$$

Here, $I_{\text{ob}}(\mathbf{r})$ describes the attenuation due to the object. It should be noted that the above expression only models the coherent flow of X-rays though the sample. We can now combine this with the Fokker-Planck equation for a phase object, Eqn. (1), to give the Fokker-Planck equation for an attenuating object as:

$$I_R(\mathbf{r})I_{\text{ob}}(\mathbf{r}) - I_S(\mathbf{r}) = \frac{\Delta}{k}\nabla_\perp \cdot [I_R(\mathbf{r})I_{\text{ob}}(\mathbf{r})\nabla_\perp \phi_{\text{ob}}(\mathbf{r})] - \Delta\nabla_\perp^2 \left[D_{\text{eff, Atten}}(\mathbf{r};\Delta) I_R(\mathbf{r})I_{\text{ob}}(\mathbf{r})\right]. \tag{3}$$

This forward-finite-difference continuity equation is formulated on the basis of local energy conservation within the system. The first term on the right-hand side describes coherent energy flow, with the second describing the diffusive component. The coherent term models local absorption, lensing and prism-like effects,[32] which are also seen in the transport-of-intensity equation.[8] The diffusion term describes the position-dependent local blurring which is associated with the SAXS fans at the exit surface of the object. Here, we remind the reader that the position-dependent SAXS fans are approximated as rotationally symmetric.

We now assume that the effective DF signal, $D_{\text{eff, Atten}}(\mathbf{r};\Delta)$, is a slowly varying function of the transverse positions, so that it approximately commutes with the transverse Laplacian operator. Moreover, we can neglect the transverse spatial derivatives of $D_{\text{eff, Atten}}(\mathbf{r};\Delta)$ as they will be small compared to the retained terms. Several components arise when the second derivative of the second term in Eqn. (3) is evaluated. Many of these can be neglected, using an approximation employed by Pavlov *et al.*[52,58]: an average, of the scalar product of a rapidly

varying vector field with a more slowly changing gradient of the product of two functions, can be neglected. Then,

$$\frac{I_S(\mathbf{r})}{I_R(\mathbf{r})} = I_{\text{ob}}(\mathbf{r}) - \frac{\Delta}{k}\nabla_\perp \cdot [I_{\text{ob}}(\mathbf{r})\nabla_\perp \phi_{\text{ob}}(\mathbf{r})] + \frac{\Delta D_{\text{eff, Atten}}(\mathbf{r};\Delta) I_{\text{ob}}(\mathbf{r})\nabla_\perp^2 I_R(\mathbf{r})}{I_R(\mathbf{r})} + \Delta D_{\text{eff, Atten}}(\mathbf{r};\Delta)\nabla_\perp^2 I_{\text{ob}}(\mathbf{r}). \quad (4)$$

We proceed by using the projection approximation for a single-material object,[59]

$$\phi_{\text{ob}}(\mathbf{r}) = -k\delta t(\mathbf{r}), \quad (5)$$

$$I_{\text{ob}}(\mathbf{r}) = e^{-2k\beta t(\mathbf{r})} = e^{-\mu t(\mathbf{r})}, \quad (6)$$

where $\mu = 2k\beta$ is the linear attenuation coefficient of the single-material object, and $t(\mathbf{r})$ is the projected thickness of the object along the direction of the X-rays, to give:

$$\frac{I_S(\mathbf{r})}{I_R(\mathbf{r})} = \left(1 - \frac{\gamma\Delta}{2k}\nabla_\perp^2\right) I_{\text{ob}}(\mathbf{r}) + \frac{\Delta D_{\text{eff, Atten}}(\mathbf{r};\Delta) I_{\text{ob}}(\mathbf{r})\nabla_\perp^2 I_R(\mathbf{r})}{I_R(\mathbf{r})} + \Delta D_{\text{eff, Atten}}(\mathbf{r};\Delta)\nabla_\perp^2 I_{\text{ob}}(\mathbf{r}). \quad (7)$$

This expression models the forward-problem of encoding a given well-resolved reference speckle field by putting an attenuating object in the beam path, where $\gamma = \delta/\beta$.

We now turn to the inverse problem. Define the additional functions:

$$G_1(\mathbf{r}) = \left(1 - \frac{\gamma\Delta}{2k}\nabla_\perp^2\right) I_{\text{ob}}(\mathbf{r}) + \Delta D_{\text{eff, Atten}}(\mathbf{r};\Delta)\nabla_\perp^2 I_{\text{ob}}(\mathbf{r}), \quad (8)$$

$$G_2(\mathbf{r}) = \Delta D_{\text{eff, Atten}}(\mathbf{r};\Delta) I_{\text{ob}}(\mathbf{r}), \quad (9)$$

$$G(\mathbf{r}) = \left(1 - \frac{\gamma\Delta}{2k}\nabla_\perp^2\right) I_{\text{ob}}(\mathbf{r}). \quad (10)$$

The function $G(\mathbf{r})$, which describes the coherent component of the optical flow, can be written in terms of the defined functions $G_1(\mathbf{r})$ and $G_2(\mathbf{r})$. That is, we apply the Laplacian operator to $G_2(\mathbf{r})$, once again assuming $D_{\text{eff, Atten}}(\mathbf{r};\Delta)$ to be slowly varying, to give:

$$\nabla_\perp^2 G_2(\mathbf{r}) = \Delta D_{\text{eff, Atten}}(\mathbf{r};\Delta)\nabla_\perp^2 I_{\text{ob}}(\mathbf{r}). \quad (11)$$

Hence,

$$G(\mathbf{r}) = G_1(\mathbf{r}) - \nabla_\perp^2 G_2(\mathbf{r}). \quad (12)$$

Eqn. (7) can now be expressed in terms of the defined functions $G_1(\mathbf{r})$ and $G_2(\mathbf{r})$, to give:

$$\frac{I_S(\mathbf{r})}{I_R(\mathbf{r})} = G_1(\mathbf{r}) + \frac{G_2(\mathbf{r})\nabla_\perp^2 I_R(\mathbf{r})}{I_R(\mathbf{r})}. \quad (13)$$

It is important to note here that the functions $G_1(\mathbf{r})$ and $G_2(\mathbf{r})$ are independent of the illuminating speckle field, hence they are unaffected by the transverse position of the speckle-generating mask. Hence, if two independent measurements of $I_S(\mathbf{r})$ and $I_R(\mathbf{r})$ are taken, e.g., by using two different positions of the mask, a system of linear equations is obtained. These linear equations can be solved for the attenuation term, $I_{\text{ob}}(\mathbf{r})$, and the effective DF signal, $D_{\text{eff, Atten}}(\mathbf{r};\Delta)$.

Specifically, if $I_{S1,S2}(\mathbf{r})$,and $I_{R1,R2}(\mathbf{r})$ denote the sample image, and well resolved speckle image for positions *1* and *2* of the mask, respectively,

$$\begin{cases} \frac{I_{S1}(\mathbf{r})}{I_{R1}(\mathbf{r})} = G_1(\mathbf{r}) + \frac{G_2(\mathbf{r})\nabla_\perp^2 I_{R1}(\mathbf{r})}{I_{R1}(\mathbf{r})}, \\ \\ \frac{I_{S2}(\mathbf{r})}{I_{R2}(\mathbf{r})} = G_1(\mathbf{r}) + \frac{G_2(\mathbf{r})\nabla_\perp^2 I_{R2}(\mathbf{r})}{I_{R2}(\mathbf{r})}. \end{cases} \quad (14)$$

Solving these equations gives:

$$G_1(\mathbf{r}) = \frac{I_{S1}(\mathbf{r})}{I_{R1}(\mathbf{r})} - \frac{G_2(\mathbf{r})\nabla_\perp^2 I_{R2}(\mathbf{r})}{I_{R2}(\mathbf{r})}, \tag{15}$$

$$G_2(\mathbf{r}) = \frac{I_{R1}(\mathbf{r})I_{S2}(\mathbf{r}) - I_{R2}(\mathbf{r})I_{S1}(\mathbf{r})}{I_{R1}(\mathbf{r})\nabla_\perp^2 I_{R2}(\mathbf{r}) - I_{R2}(\mathbf{r})\nabla_\perp^2 I_{R1}(\mathbf{r})}. \tag{16}$$

Using the approach presented in Paganin *et al.*,[7] and the definition of $G_2(\mathbf{r})$, the effective DF signal $D_{\text{eff, Atten}}(\mathbf{r};\Delta)$ and projected thickness $t(\mathbf{r})$, of a SAXS-inducing attenuating object, are given as:

$$t(\mathbf{r}) = \frac{-1}{\mu}\log_e \mathcal{F}^{-1}\left[\frac{\mathcal{F}\,G(\mathbf{r})}{1+\gamma\Delta k\pi(u^2+v^2)}\right], \tag{17}$$

$$D_{\text{eff, Atten}}(\mathbf{r};\Delta) = \frac{G_2(\mathbf{r})}{\Delta I_{ob}(\mathbf{r})}. \tag{18}$$

In Eqn. (17), $\mathcal{F}$ is denotes Fourier transformation with respect to x and y, for which the corresponding Fourier-space variables are u and v, respectively. It should be highlighted that the expression for the effective DF of an attenuating object, namely Eqn. (18) above, is equivalent to Eqn. (7) from Pavlov *et al.*,[52] for the special case of a phase object.

2.2 Numerical Stabilisation of Recovered Dark-Field Images

DF images are intrinsically noisy[32,33] in the sense that the diffuse scattering which underpins them is due to extremely small unresolved spatially-random features within the sample. This leads to finely-fluctuating unresolved speckle variations over individual pixels. By spatially averaging these high-frequency variations across pixels, the DF signal is obtained. Gureyev *et al.*[33] developed a model based on the assumption of a single-material sample for which the projected linear attenuation coefficient, $\mu_{\text{p}}(\mathbf{r})$, is a composite of a rapidly varying component $\mu_{\text{fast,p}}(\boldsymbol{r})$, and a slowly-varying component $\mu_{\text{slow,p}}(\boldsymbol{r})$:

$$\mu_{\text{p}}(\mathbf{r}) = \mu_{\text{fast,p}}(\mathbf{r}) + \mu_{\text{slow,p}}(\mathbf{r}). \tag{19}$$

Here, $\mu_{\text{slow,p}}(\boldsymbol{r})$ results from density variations over length scales larger than the pixel size, which hence can be resolved in a typical phase-contrast image. Conversely, $\mu_{\text{fast,p}}(\boldsymbol{r})$ is associated with unresolved microstructure in the sample, which fluctuates rapidly throughout the sample, and hence across one detector pixel. The spatially-averaged fast-varying component of the projected linear attenuation coefficient, $\overline{\mu_{\text{fast,p}}(\mathbf{r})}$, is connected to the effective DF signal by:[33]

$$D_{\text{eff}}(\mathbf{r};\Delta) = \frac{\delta}{\beta k}\,\overline{|\mu_{\text{fast,p}}(\mathbf{r})|^2}. \tag{20}$$

Here, the overline denotes spatial averaging over a single detector pixel. Since the above expression is obtained via a spatial average of an intrinsically rapidly-varying and often-spatially-random quantity, the effective DF signal is typically inherently noisy.

This "intrinsic noise" is closely related to the evident numerical division-by-zero instability in Eqn. (18). To deal with this instability, we propose two alternative approaches to numerically stabilise this expression. Each is considered in turn, below.

Method i) **Tikhonov Regularisation**: This is a well known mathematical technique[60–62] and can easily be implemented by making the replacement, for any numerator and denominator $A(\mathbf{r})$ and $B(\mathbf{r})$, of:

$$\frac{A(\mathbf{r})}{B(\mathbf{r})} \to \frac{A(\mathbf{r})B(\mathbf{r})}{[B(\mathbf{r})]^2+\epsilon}. \tag{21}$$

Here, ϵ is a positive regularisation parameter.

Method ii) **Weighted-Determinants**: This method utilises the determinant of the system of linear equations, Eqn. (14). Moreover, the determinant is used as a weighting factor for the appropriate pairs of mask positions, a and b. The determinant of the system of linear equations is:

$$\mathrm{Det}_{a,b}(\mathbf{r}) = \frac{\nabla_\perp^2 I_{Rb}(\mathbf{r})}{I_{Rb}(\mathbf{r})} - \frac{\nabla_\perp^2 I_{Ra}(\mathbf{r})}{I_{Ra}(\mathbf{r})}. \tag{22}$$

The determinant of a system of linear equations characterizes the stability of the solution. A system of linear equations has a unique and stable solution if the determinant is nonzero. Therefore, as the determinant approaches zero, the solution becomes unstable. The determinant of Eqn. (14) is an array equal to the size of the input projection images, and its elements will give a pixel-wise measure of how much to "trust" the corresponding element in the DF image. Then, given N different mask positions, we can calculate $[N(N-1)/2]$ effective DF projection images, for each distinct pair of mask positions. The determinant of the appropriate system of linear equations can then be calculated using Eqn. (22). The effective DF projection images can subsequently be weighted by their appropriate squared determinant, summed, and normalised to give what we term the "Weighted Determinant" effective DF projection image, $WD[D_{eff}((\boldsymbol{r});\Delta)]$. To demonstrate this approach, we present the weighted-determinant expression for three transverse positions of the mask, $N = 3$, however this can be easily extended to a larger number of mask positions:

$$\mathrm{WD}\left[D_{\mathrm{eff}}(\mathbf{r};\Delta)\right] = \frac{\left|\mathrm{Det}_{1,2}(\mathbf{r})\right|^2 D_{\mathrm{eff}}^{1,2}(\mathbf{r}) \;+\; \left|\mathrm{Det}_{2,3}(\mathbf{r})\right|^2 D_{\mathrm{eff}}^{2,3}(\mathbf{r}) \;+\; \left|\mathrm{Det}_{1,3}(\mathbf{r})\right|^2 D_{\mathrm{eff}}^{1,3}(\mathbf{r})}{\left|\mathrm{Det}_{1,2}(\mathbf{r})\right|^2 \;+\; \left|\mathrm{Det}_{2,3}(\mathbf{r})\right|^2 \;+\; \left|\mathrm{Det}_{1,3}(\mathbf{r})\right|^2}. \tag{23}$$

3. EXPERIMENTAL DATA / PROCEDURE

The experimental X-ray data analyzed throughout the presented work was collected at the Imaging and Medical Beamline (IMBL) at the Australian Synchrotron in Melbourne. This set of SBXI data was collected in hutch 3B, which is often used for large-sample X-ray imaging and computed tomography, due to its large X-ray beam-size. A Ruby detector[63] was used, which has a single pco.edge sensor and a lens-coupled scintillator. The detector's pixelation is 2560×2160, with an effective pixel size of 12.5μm. The distance between the source and beam entrance window for hutch 3B, *smd*, was 135.8m, the distance between the mask and sample, *msd*, was 1.019m, and the propagation distance, $sdd = \Delta$, between the sample and detector, was 2.0m. The speckle-generating mask had a typical grain size of 30–45μm. The position of the mask was transversely shifted, in the direction perpendicular to the beam, to acquire a total of six different sets of raw intensity projection data.

The sample investigated throughout was a wood sample, as shown in Fig. 1. This sample has three different wood types, *i) - iii)*, mounted onto a metal cylindrical disk. The exact wood type of these samples was unknown, however, key characteristics can be observed from Fig. 1.

SBXI was carried out on the wood sample with a monochromatic X-ray beam of energy 30keV. Raw intensity projection data were collected, namely three data sets: sample projections, mask-reference projections, and dark-current projections. Sample projections included intensity variations arising from phase and attenuation differences introduced by both the sample and specified mask, whereas the reference-speckle projections showed just the image of the mask. The dark-current projection images were collected in the absence of X-rays, used to correct for the detector. The acquired projection images were then processed within a Python3 script to calculate the attenuation, projected thickness, and DF images.

The projected thickness, and hence attenuation, of the wood sample was calculated using Eqn. (18) from Pavlov *et al.*,[58] with $\gamma = 2990$, assuming a generic composition of wood. The phase-object approximation for the effective DF image was then calculated using a Tikhonov-Regularised weighted-determinant variant of Eqn. (7), that is, the two methods in conjunction, from Pavlov,[52] or equivalently,

$$D_{\mathrm{eff,\ Phase}}(\mathbf{r};\Delta) = \frac{G_2(\mathbf{r})}{\Delta}, \tag{24}$$

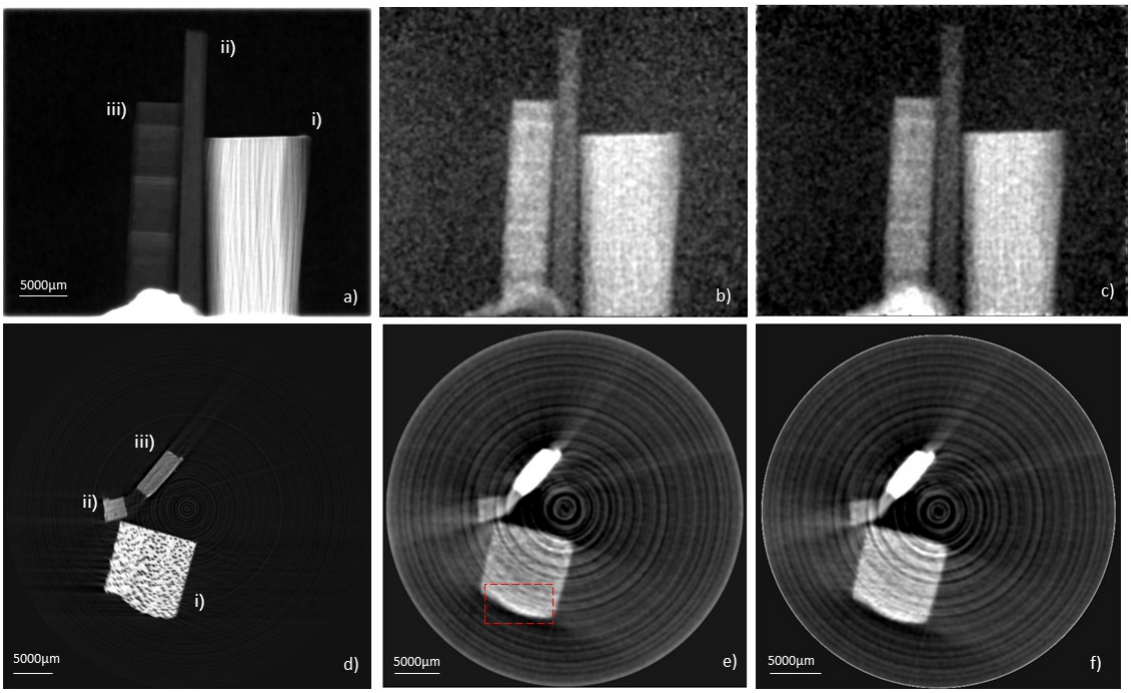

Figure 2. *Top row: Projection images, in the direction of the optical axis, z, of (a) projected-thickness, (b) effective dark-field signal generated using a phase-object approximation, and (c) attenuating-object approximation of the wood sample. Bottom row: Computed-Tomography (CT) reconstructions of (d) attenuation coefficient, $\beta(\boldsymbol{r})$, (e) phase-object approximation for the dark-field, and (f) attenuating-object approximation for the dark-field. Wood labelling, i) – iii), refers to that in Fig. 1.*

as derived in this paper. From there, the attenuating-object approximation of the DF image was calculated using, once again, a Tikhonov-regularised weighted-determinant form of Eqn. (18). As we had SBXI data for six different well-resolved reference speckle-fields, $N = 6$ in Eqn. (23), these were all utilized to calculate the effective DF. All of the speckle-fields were included to maximise the DF signal quality and robustness to noise, following Pavlov *et al.*[52]

4. DISCUSSION / ANALYSIS

We have experimentally implemented the phase-object approximation to MIST[52] and then extended this to consider a monomorphous attenuating object, by utilizing the already-presented multimodal X-ray Fokker-Planck based speckle tracking approach.[32] Figures 2b and 2c demonstrate how the proposed extension of MIST[52] to consider an attenuating-object, rather than a phase-object, more accurately models objects that attenuate the X-ray beam significantly. An example of this is the feature at the bottom centre of Fig. 2b and 2c, namely Blu Tack, which has strong attenuating and small-angle scattering characteristics. In the phase-object approximation (see Fig. 2b), the effective DF is significantly suppressed in inner regions of the wood samples due to strong X-ray attenuation. However, this effective DF is corrected in the attenuating-object approximation (see Fig. 2c) as the object attenuation-term, $I_{ob}(\mathbf{r})$¸ has been considered.

The effective DF projection images have been numerically stabilised using the "Weighted-Determinant" approach, as well as Tikhonov regularisation, as given by Eqs. (21) and (23). We utilized the entire data set of six transverse mask positions, $N = 6$. However, fewer mask positions were also investigated using the same approach, and the results agreed with that of Pavlov *et al.*,[52,53] demonstrating that two mask positions are sufficient

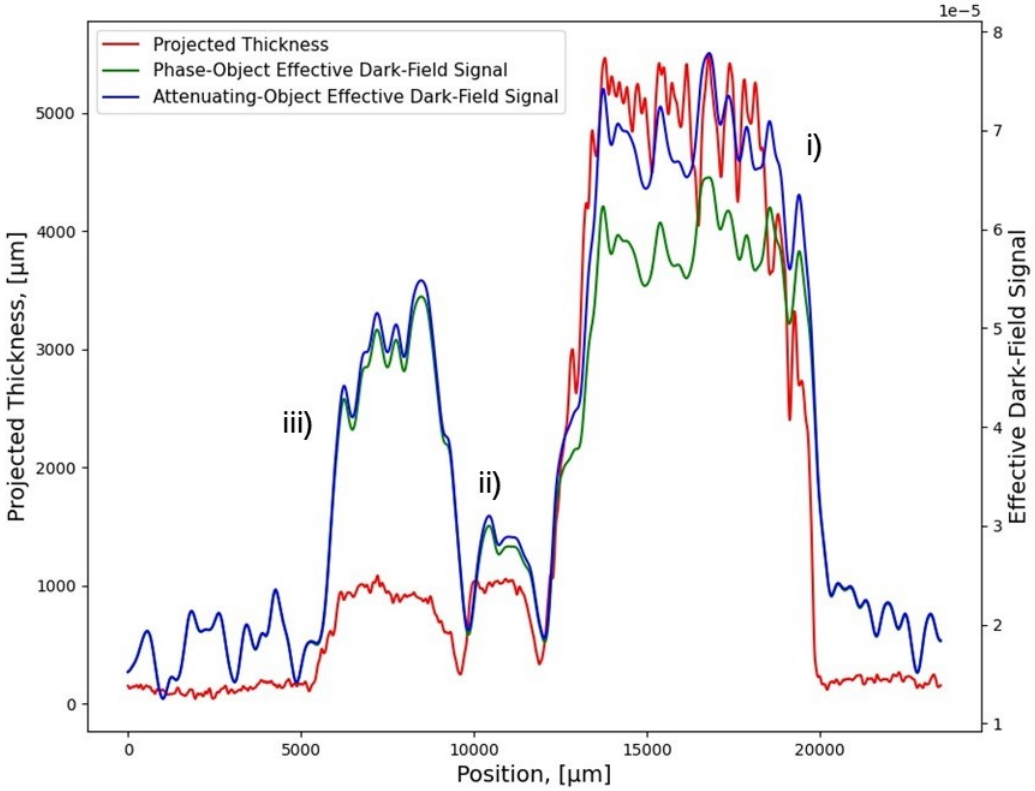

Figure 3. *Line profiles across taken across each of the wood samples in the projection images of (red) projected thickness, (green) phase object approximation dark-field image, and (blue) attenuating object approximation dark-field image. Wood labelling, i) – iii), refers to that in Fig. 1.*

to obtain a DF signal. The quality of the reconstructed DF signal was clearly improved using the Tikhonov-regularised weighted-determinant method. This optimisation of effective DF projection images (Figs. 2b and 2c) then allowed standard CT algorithms to be used to reconstruct axial slices (Figs. 2e and 2f). Here, XTRACT[64] software was used to implement a filtered-backprojection CT reconstruction algorithm, with a Hamming filter being used for noise suppression.[65] The weighted-determinant variant of numerical stabilisation was less computationally expensive, giving a reduction of a factor of 100 in computation time, compared to other trialled techniques, for example having a pixel-wise matrix inversion to obtain the solution in a least-squares[66] sense.

Figures 2 and 3 demonstrate the differing structural information obtained in bright-field, standard PCI, and DF imaging, and also how the presented monomorphous attenuating-object description compares to the previously published[52] phase-object approach. The projected thickness, Fig. 2a, displays the fibre-like features in the wood: these run horizontally in sample *iii)* and vertically in sample *i)*. Such features are also resolvable in the DF images, Fig. 2b and 2c, alongside further variations in structural characteristics. It is interesting to note that while sample *iii)* has the weakest contrast of the three samples in the attenuation coefficient image in Fig. 2d, this sample has the strongest contrast of the three samples in the DF images shown in Fig. 2e and Fig. 2f. The power of DF imaging is accentuated in Fig. 2, particularly the complementary information for samples *ii)* and *iii)*. Moreover, although the projected thickness is equal for these two samples, sample *iii)* has a factor of 2 greater effective DF signal than *ii)*. These characteristics are also shown in the CT reconstructions. Indeed, there is further structural information about the wood sample that is revealed in the CT reconstructions and not seen in the projection images. For example, as previously mentioned, in the axial slice shown in Fig. 2, sample *ii)* has the largest effective DF signal, yet the lowest attenuation coefficient, $\beta(\mathbf{r})$. An unseen structural feature

also appears in the DF-CT reconstruction of wood sample *i)* that is not in the PC-CT, marked in red.

Equation 18 was used to calculate the effective DF signal, shown in Fig. 2, which was derived under the assumption that the SAXS fans emanating from the exit-surface of the sample are rotationally symmetric. However, the sample studied within, wood, typically has anisotropic scattering structures, and thus one might think that the key assumption (i.e., rotational symmetry of the position-dependent SAXS fans that underpin the DF signal) is violated. However, we see in Figs. 2 and 3, that the isotropic attenuating-object approximation, which improves upon the isotropic phase-object approximation, extracts a first approximation (i.e., rotationally symmetric) of the dark-field signal that well represents the wood sample. Stated differently, the locally-elliptical position-dependent SAXS fans may be reasonably approximated as rotationally symmetric, to give lowest-order position-dependent information regarding this scattering channel. This suggests that the formalism presented in our paper is capable of providing directionally-averaged DF information, for objects that may violate the underlying assumptions of rotationally-symmetric position-dependent SAXS fans.

The qualitative points-of-difference between these images, numerical stability, low computational time, simple experimental set-up, and low object X-ray exposure showcases the broad applicability and viability of this technique. As the Fokker-Planck SBXI formalism[32] is based on several assumptions, CT artefacts are seen in the reconstructions: streaking and ring-artefacts. Typical artefact reduction techniques[67,68] in CT reconstruction may be successful within this application, however, this is an avenue for further work.

5. CONCLUSION

We have developed a monomorphous attenuating-object variant of the phase-object MIST X-ray speckle-tracking method proposed in 2020 by Pavlov *et al.*[52] Our method has been demonstrated on experimental data to achieve speckle-based X-ray DF tomography. A numerical stabilisation approach, namely the "Weighted Determinant" method, together with Tikhonov Regularisation, was used to stabilise the intrinsic noise of DF images. These reconstructions are based on six sets of images acquired at different transverse positions of the speckle mask. However, reconstructions based on two images, as reported also by Pavlov *et al.*,[52] give comparable reconstructions, albeit with higher noise on account of the smaller number of measurements that are required.

DISCLOSURES

All authors within the presented manuscript report no relevant conflicts of interest or financial interests with respect to this work.

ACKNOWLEDGMENTS

This research was undertaken on the Imaging and Medical beamline (proposal AS193/IMBL/15230) at the Australian Synchrotron, part of ANSTO. The authors also acknowledge the University of Canterbury for awarding a Doctoral Scholarship to S. J. Alloo. This paper is based on a submitted SPIE conference proceeding paper.[69]

REFERENCES

[1] Röntgen, W. C. "Über eine neue Art von Strahlen", *Sitzungsberichte der Physikalisch-medizinischen Gesellschaft zu Würzburg* Vol. 28, 132–141 (1895).

[2] Pelliccia, D., Kitchen, M. J. & Morgan, K. S. "Handbook of X-ray Imaging: Physics and Technology, ch. 49, Theory of X-ray Phase-Contrast Imaging", *CRC Press* (2018).

[3] Snigirev, A., Snigireva, I., Kohn, V., Kuznetsov, S., & Schelokov, I. "On the possibilities of X-ray phase contrast microimaging by coherent high-energy synchrotron radiation", *Rev. Sci. Instrum.* Vol. 66, 5486–5492 (1995).

[4] Wilkins, S. W., Gureyev, T. E., Gao, D., Pogany, A., & Stevenson, A. W. "Phase-contrast imaging using polychromatic hard X-rays", *Nature* Vol. 384, 335–338 (1996).

[5] Nugent, K. A., Gureyev, T. E., Cookson, D. F., Paganin, D., & Barnea, Z. "Quantitative phase imaging using hard X-rays", *Phys. Rev. Lett.* Vol. 77, 2961-2964 (1996).

[6] Cloetens, P., Barrett, R., Baruchel, J., Guigay, J.-P. & Schlenker, M. "Phase objects in synchrotron radiation hard x-ray imaging", *J. Phys. D: Appl. Phys.* Vol. 29, 133-146 (1996).

[7] Paganin, D., Mayo, S. C., Gureyev, T. E., Miller, P. R., & Wilkins, S. W. "Simultaneous phase and amplitude extraction from a single defocused image of a homogeneous object", *J. Microsc.* Vol. 206, Pt 1, Pg. 33-40 (2002).

[8] Teague, M. R. "Deterministic phase retrieval: a Green's function solution", *J. Opt. Soc. Am. A.* Vol. 73, 1434-1441 (1983).

[9] David, C., Nöhammer, B., Solak, H. H., & Ziegler, E. "Differential x-ray phase contrast imaging using a shearing interferometer", *Appl. Phys. Lett.* Vol. 81, 3287-3289 (2002).

[10] Momose, A., Kawamoto, S., Koyama, I., Hamaishi, Y., Takai, K. & Suzuki, Y. "Demonstration of X-ray Talbot interferometry", *Jpn J. Appl. Phys.* Vol. 42, L866-L868 (2003).

[11] Weitkamp, T., Nöhammer, B., Diaz, A., David, C., & Ziegler, E. "X-ray wavefront analysis and optics characterization with a grating interferometer", *Appl. Phys. Lett.* Vol. 86, 054101 (2005).

[12] Weitkamp, T., Diaz, A., David, C., Pfeiffer, F., Stampanoni, M., Cloetens, P. & Ziegler, E. "X-ray phase imaging with a grating interferometer", *Opt. Express* Vol. 13, 6295-6304 (2005).

[13] Pfeiffer, F., Weitkamp, T., Bunk, O. & David, C. "Phase retrieval and differential phase-contrast imaging with low-brilliance X-ray sources", *Nat. Phys.* Vol. 2, 258-261 (2006).

[14] Momose, A., Yashiro, W. , Takeda, Y., Suzuki, Y. & Hattori, T. "Phase tomography by X-ray Talbot interferometry for biological Imaging", *Jpn J. Appl. Phys.* Vol. 45, 5254-5262 (2006).

[15] Takeda, Y., Yashiro, W. , Suzuki, Y., Aoki, S., Hattori, T. & Momose, A. "X-Ray phase imaging with single phase grating", *Jpn J. Appl. Phys.* Vol. 46, L89-L91 (2007).

[16] Xi, Y., & Zhao, J. "Fast grating-based X-ray phase-contrast tomosynthesis", *Annu. Int. Conf. IEEE Eng. Med. Biol. Soc.* PMID: 24110189, 2320-2323 (2013).

[17] Bonse, U. & Hart, M. "An x-ray interferometer", *Appl. Phys. Lett.* Vol. 6, 155–156 (1965).

[18] Momose, A. "Demonstration of phase-contrast X-ray computed tomography using an X-ray interferometer", *Nucl. Instrum. Methods Phys. Res. A* Vol. 352, 622-628 (1995).

[19] Wen, H., Gomella, A. G., Patel, A., Wolfe, D. E., Lynch, S. K., Xiao, X., & Morgan, N. "Boosting phase contrast with a grating Bonse–Hart interferometer of 200 nanometre grating period", *Philos. Trans. A. Math. Phys. Eng. Sci.* Vol. 372, 20130028 (2010).

[20] Olivo, A. & Speller, R. "A coded-aperture technique allowing x-ray phase contrast imaging with conventional sources", *Appl. Phys. Lett.* Vol. 074106, 074106 (2007).

[21] Olivo, A., Arfelli, F., Cantatore, G., Longo, R., Menk, R. H., Pani, S., Prest, M., Poropat, P., Rigon, L., Tromba, G., Vallazza, E., & Castelli, E. "An innovative digital imaging set-up allowing a low-dose approach to phase contrast applications in the medical field", *Med. Phys.* Vol. 28, 1610-1619 (2001).

[22] Goetz, K., Kalashnikov, M. P., Mikhailov, Y. A., Sklizkov, G. V., Fedotov, S. I., Foerster, E., & Zaumseil, P. "Measurement of parameters of shell targets for laser fusion with the use of X-ray schlieren technique", *Sov. J. Quant. Electron.* Vol. 9, 607–610 (1979).

[23] Somenkov, V. A., Tkalich, A. K. & Shil'shtein, S. Sh. "Refraction contrast in x-ray introscopy", *Sov. Phys. Tech. Phys.* Vol. 36, 1309-1311 (1991).

[24] Ingal, V. N., & Beliaevskaya, E. A. "X-ray plane-wave topography observation of the phase contrast from a noncrystalline object", *J. Phys. D: Appl. Phys.* Vol. 28, 2314–2317 (1995).

[25] Davis, T. J., Gao, D., Gureyev, T. E., Stevenson, A. W. & Wilkins, S. W. "Phase-contrast imaging of weakly absorbing materials using hard X-rays", *Nature* Vol. 373, 595-598 (1995).

[26] Wernick, M. N., Wirjadi, O., Chapman, D., Zhong, Z., Galatsanos, N. P., Yang, Y., Brankov, J. G., Oltulu, O., Anastasio, M. A., & Muehleman, C. "Multiple-image radiography", *Phys. Med. Biol.* Vol. 48, 3875–3895 (2003).

[27] Berujon, S., Ziegler, E., Cerbino, R., & Peverini, L. "Two-Dimensional X-Ray Beam Phase Sensing", *Phys. Rev. Lett.* Vol. 108, 158102 (2012).

[28] Morgan, K. S., Paganin, D. M., & Siu, K. K. W. "X-ray phase imaging with a paper analyser", *Appl. Phys. Lett.* Vol. 100, 124102 (2012).

[29] Zdora, M.-C. "State of the art of X-ray speckle-based phase-contrast and dark-field imaging", *J. Imaging*, Vol. 4, 60 (2018).

[30] Kratky, O. and Glatter, O. "Small Angle X-ray Scattering", *Academic Press* (1982).
[31] Sabatier, P. C. "Past and future of inverse problems", *J. Math. Phys.* Vol. 41, 4082-4124 (2000).
[32] Paganin, D. M., & Morgan, K. S. "X-ray Fokker-Planck equation for paraxial imaging", *Sci. Rep.* Vol. 9, 17537 (2019).
[33] Gureyev, T. E., Paganin, D. M., Arhatari, B., Taba, S. T., Lewis, S., Brennan, P. C., & Quiney, H. M. "Dark-field signal extraction in propagation-based phase-contrast imaging", *Phys. Med. Biol.* Vol. 65, 215029 (2020).
[34] Pfeiffer, F., Bech, M., Bunk, O., Kraft, P., Eikenberry, E. F., Brönnimann, C., Grünzweig, C., & David, C. "Hard-X-ray dark-field imaging using a grating interferometer", *Nature. Mat.* Vol. 7, 2, 134-137 (2008).
[35] Velroyen, A., Yaroshenko, A., Hahna, D., Fehringer, A., Tapfer, A., Müller, M., Noël, P. B., Pauwels, B., Sasov, A., Yildirimd, A. Ö., Eickelberg, E., Hellbach, K., Auweter, S. D., Meinel, F. G., Reiser, M. F., Bech, M., & Pfeiffer, F. "Grating-based X-ray dark-field computer tomography of living mice", *E. Bio. Medicine* Vol. 2, 1500–1506 (2015).
[36] Pfeiffer, F., Bech, M., Bunk, O., Donath, T., Henrich, B., Kraft, P., & David, C. "X-ray dark-field and phase-contrast imaging using a grating interferometer", *J. Appl. Phys.* Vol. 105, 102006 (2009).
[37] Yaroshenko, A., Hellbach, K., Bech, M., Grandl, S., Reiser, M. F., Pfeiffer, F., & Meinel, F. G. "Grating-based X-ray dark-field imaging: a new paradigm in radiography", *Curr. Radiol. Rep.* Vol 2, 57 (2014).
[38] Endrizzi, M., Murat, B. I. S., Fromme, P., & Olivo, A. "Edge-illumination X-ray dark-field imaging for visualising defects in composite structures", *Compos. Struct.* Vol. 145, 895-899 (2015).
[39] Matsunaga, N., Yano, K., Endrizzi, M., & Olivo, A. "Detection of individual sub-pixel features in edge-illumination x-ray phase contrast imaging by means of the dark-field channel", *J. Phys. D: Appl. Phys.* Vol. 53, 095401 (2019).
[40] Pagot, E., Cloetens, P., Fiedler, S., Bravin, A., Coan, P., Baruchel, J., Härtwig, J., & Thomlinson, W. "A method to extract quantitative information in analyzer-based x-ray phase contrast imaging", *Appl. Phys. Lett.* Vol. 82, 3421-3423 (2003)
[41] Majidi, K., Brankov, J. G., & Wernick, M. N. "Sampling Strategies in Multiple-Image Radiography", *2008 5th IEEE International Symposium on Biomedical Imaging: From Nano to Macro*, 688-691 (2008).
[42] Ando, M., Sunaguchi, N., Shimao, D., Pan, A., Yuasa, T., Mori, K., Suzuki, Y., Jin, G., Kim, J., Lim, J., Seo, S., Ichihara, S., Ohura, N., & Gupta, R. "Dark-Field Imaging: Recent developments and potential clinical applications", *Phys. Medica* Vol. 32, 1801-1812 (2016).
[43] Ando, M., Nakao, Y., Jin, G., et al. "Improving contrast and spatial resolution in crystal analyser-based X-ray dark-field imaging: Theoretical considerations and experimental demonstration", *Med. Phys.* Vol. 47, 5505-5513 (2020).
[44] Bennett, E. E., Kopace, R., Stein, A. F., & Wen, H. "A grating-based single-shot x-ray phase contrast and diffraction method for in vivo imaging", *Med. Phys.* Vol. 37, 6047–6054 (2010).
[45] Morgan, K. S., Paganin, D. M. & Siu, K. K. W. "Quantitative single-exposure x-ray phase contrast imaging using a single attenuation grid", *Opt. Express* Vol. 19, 19781–19789 (2011).
[46] Kitchen, M. J., Pavlov, K. M., Hooper, S. B., Vine, D. J., Siu, K., Wallace, M. J., Siew, M. L. L., Yagi, N., Uesugi, K., & Lewis, R. A. "Simultaneous acquisition of dual analyser-based phase contrast X-ray images for small animal imaging", *Eur. J. Radiol.* Vol. 68, S49-S53 (2008).
[47] Kitchen, M. J., Paganin, D. M., Uesugi, K., Allison, B. J., Lewis, R. A., Hooper, S. B., & Pavlov, K. M. "X-ray phase, absorption and scatter retrieval using two or more phase contrast images", *Opt. Express* Vol. 18, 19994-20012 (2010).
[48] Kitchen, M. J., Paganin, D. M., Uesugi, K., Allison, B. J., Lewis, R. A., Hooper, S. B., & Pavlov, K. M. "Phase contrast image segmentation using a Laue analyser crystal", *Phys. Med. Biol.* Vol. 56, 515-534 (2011).
[49] Zdora, M.-C., Thibault, P., Zhou, T., Koch, F. J., Romell, J., Sala, S., Last, A., Rau, C., & Zanette, I. "X-ray phase-contrast imaging and metrology through unified modulated pattern analysis", *Phys. Rev. Lett.* Vol. 118, 203903 (2017)
[50] Zanette, I., Zhou, T., Burvall, A., Lundström, U., Larsson, D. H., Zdora, M., Thibault, P., Pfeiffer, F., & Hertz, H. M. "Speckle-based x-ray phase-contrast and dark-field imaging with a laboratory source", *Phys. Rev. Lett.* Vol. 112, 253903 (2014).

[51] Berujon, S., & Ziegler, E. "X-ray multimodal tomography using speckle-vector tracking", *Phys. Rev. Appl.*, Vol. 5, 044014 (2016).

[52] Pavlov, K. M., Paganin, D. M., Li, H., Berujon, S., Rougé-Labriet, H. T., & Brun, E. "X-ray multi-modal intrinsic-speckle-tracking", *J. Opt.* Vol. 22, 125604 (2020).

[53] Pavlov, K. M., Paganin, D. M., Morgan, K. S., Li, H., Berujon, S., Quénot, L., & Brun, E. "Directional dark-field implicit x-ray speckle tracking using an anisotropic-diffusion Fokker-Planck equation", *arXiv*, preprint 2105.10693 (2021).

[54] Morgan, K. S., & Paganin, D. M. "Applying the Fokker-Planck equation to grating-based x-ray phase and dark-field imaging", *Sci. Rep.* Vol. 9, 17465 (2019).

[55] Risken, H. "The Fokker–Planck Equation: Methods of Solution and Applications: 2nd edn", *Springer* (1989).

[56] Paganin, D. M., Labriet, H., Brun, E., & Berujon, S. "Single-image geometric-flow x-ray speckle tracking", *Phys. Rev. A* Vol. 98, 053813 (2018).

[57] Willer, K., Fingerle, A. A., Gromann, L. B., De Marco, F., Herzen, J., Achterhold, K., et al. "X-ray dark-field imaging of the human lung – A feasibility study on a deceased body", *PLoS One* Vol. 13, e0204565 (2018).

[58] Pavlov, K. M., Li, H. T., Paganin, D. M., Berujon, S., Rougé-Labriet, & Brun, E. "Single-shot x-ray speckle-based imaging of a single-material object", *Phys. Rev. Appl.* Vol. 13, 054023 (2020).

[59] Paganin, D. M. "Coherent X-ray Optics", *Oxford University Press* (2006).

[60] Tikhonov, A. N., & Arsenin, V. Y. "Solution of Ill-posed Problems", *Winston & Sons* (1977).

[61] Fathi, E., & M. M., Shoja. "Deep Neutral Networks for Natural Language Processing", *Handbook of Statistics*, Vol. 38, Chapter 9, 229–316 (2018).

[62] Murli, A., D'Amore, L., & De Simone, V. "The Wiener filter and regularisation methods for image restoration problems", *Proceedings 10th International Conference on Image Analysis and Processing, Venice, Italy*, 394-399 (1999).

[63] Australian Synchrotron, ANSTO. "Preparation for imaging and computing tomography experiments". *IMBL*. Retrieved From: http://archive.synchrotron.org.au/index.php?option=com_content&view=article&id=811&catid=31&Itemid=101 (2020).

[64] Gureyev, T. E., Nesterets, Y., Ternovski, D., Thompson, D., Wilkins, S. W., Stevenson, A. W., Sakellariou, A., & Taylor, J. A. "Toolbox for advanced X-ray image processing", *Proc. SPIE*, 8141, 81410B, 81410B-14, Version 8.14.0.0 (2020).

[65] Kak, A. C., & Slaney, M. "Principles of Computerized Tomographic Imaging", *IEEE Press* (1988).

[66] Press, W. H., Teukolsky, S. A., Vetterling, W. T., & Flannery, B. P. "Numerical Recipes in FORTRAN: The Art of Scientific Computing (2nd edn)", *Cambridge University Press* (1996).

[67] Boas, F., & Fleischmann, D. "CT artifacts: Causes and reduction techniques", *Imaging Med.* Vol. 4, 2 (2012).

[68] Yang, Y., Zhang, D., Yang, F., Teng, M., Du, Y., & Huang, K. "Post-processing method for the removal of mixed ring artifacts in CT images", *Opt. Express* Vol. 28, 30362-30378 (2020).

[69] Alloo, S. J., Paganin, D. M., Morgan, K. S., Kitchen, M. J., Stevenson, A. W., Mayo, S. C., Li, H. T., Kennedy, B., Maksimenko, A., Bowden, J., & Pavlov, K. M. "Speckle-Based X-Ray Dark-Field Tomography of an Attenuating Object". *Submitted to SPIE Conf. Proc.* Vol. 11840 (2021).